TUDelft

Delft University of Technology

Direct Numerical Simulation of a Turbulent Boundary Layer over Acoustic Liners

Shahzad, Haris; Hickel, Stefan; Modesti, Davide

Important note
To cite this publication, please use the final published version (if applicable).
Please check the document version above.

Direct Numerical Simulation of a Turbulent Boundary Layer over Acoustic Liners

Haris Shahzad* and Stefan Hickel†

Aerodynamics Group, Faculty of Aerospace Engineering, Delft University of Technology, Kluyverweg 2, 2629 HS Delft, The Netherlands

and

Davide Modesti‡

Gran Sasso Science Institute, L'Aquila, 67100 Abruzzo, Italy

The nacelle of aircraft engines is coated with acoustic liners to reduce engine noise emissions. An undesirable side effect of acoustic liners is that they increase aerodynamic drag. For the first time, the authors study this drag penalty through pore-resolved direct numerical simulation (DNS) of a flat-plate zero pressure gradient turbulent boundary layer at friction Reynolds number $Re_\tau \approx 850–2600$, which is high enough to be representative of liners in operating conditions. In the configuration under scrutiny, the turbulent boundary layer experiences a step change in surface topography passing from a smooth wall to an acoustic liner array, allowing one to study the streamwise adaptation length of the boundary layer. It is found that the mean velocity profile adjusts to the new surface condition in a nearly negligible distance (less than 10 local boundary-layer thicknesses), whereas turbulent fluctuations take much longer. DNS is also performed with external acoustic noise in the form of planar monocromatic waves grazing the boundary layer with an amplitude of 150 dB. In agreement with some earlier studies, it is found that sound waves do not affect aerodynamic drag at these flow conditions.

Nomenclature

C_f	=	skin-friction coefficient
c	=	speed of sound
d	=	orifice diameter
k	=	cavity depth
L_χ	=	domain length in χ direction
M	=	Mach number
N_χ	=	grid points in χ direction
Re	=	Reynolds number
t	=	orifice thickness
u_τ	=	friction velocity
u_∞	=	freestream velocity
x_t	=	smooth-to-porous transition location
λ	=	cavity cross-section length/width
ΔU^+	=	Hama roughness function
δ	=	boundary-layer thickness
δ_v	=	viscous length scale
ν	=	kinematic viscosity
ρ	=	density
σ	=	facesheet porosity
τ_{ij}	=	Reynolds stresses
τ_w	=	wall shear stress

I. Introduction

AIRCRAFT engine noise is amongst the most relevant sources of noise during takeoff and landing. Other relevant sources include, for instance, the landing gears, flaps, and slats. To reduce noise, engine nacelles are equipped with noise control devices called acoustic liners. Acoustic liners consist of a porous facesheet and a solid backplate with a honeycomb core in between the two. They are arrays of Helmholtz resonators and exhibit a resonance frequency that can be tuned to the dominant frequency of the engine fan for engine noise reduction. Due to the passive nature of these devices and their efficacy, acoustic liners are widely used. However, the perforated facesheet acts as a rough surface, and acoustic liners, as a result, have a profound aerodynamic influence [1] and tend to increase aircraft drag. The drag increase was accepted as a necessary compromise as the need to reduce noise emissions took precedence. Therefore, acoustic liners have primarily been studied and optimized from an acoustic perspective [2,3].

The aerodynamic impact of acoustic liners has been studied considerably less, partially because of the disparity between the liner and flow length scales, which make the problem difficult to study both numerically and experimentally. The diameter of the orifices d is significant with respect to the boundary-layer thickness ($d/\delta \approx 0.1$) and much larger than the viscous length scale ($d^+ = d/\delta_v \approx 500$), where δ is the boundary-layer thickness, and $\delta_v = \nu_w/u_\tau$ is the viscous length scale based on the friction velocity $u_\tau = \sqrt{\tau_w/\rho_w}$, where ν_w, ρ_w, and τ_w are the wall kinematic viscosity, wall density, and the drag per plane area, respectively. Simultaneously satisfying these constraints on the diameter in numerical simulations or wind-tunnel experiments results in demanding computational costs and difficulties in experimental measurements. Most previous numerical studies have, thus, employed simplifying approximations such as studying a single resonator [4,5], or employing an equivalent boundary condition [6] instead of resolving the complex geometry. Tam et al. [7] studied acoustic liners subject to a mean turbulent boundary layer and an acoustic wave, assuming linearized behavior, so that the turbulent boundary layer and acoustic wave acted independently of each other. Shur et al. [8] also studied acoustic liners subjected to acoustic forcing in the presence of a turbulent boundary layer. However, Shur et al. [8] used impedance boundary conditions to resolve the acoustic liners and, similar to the work of Tam et al. [7], employed turbulence models instead of resolving the turbulent scales. More recently, Pereira et al. [9] performed experiments and large eddy simulations of acoustic waves over an acoustic liner, with and without grazing flow. They found that the effective orifice area for acoustic excitation is reduced in the presence of a grazing flow due to the formation of a quasi-steady vortex in the orifice. Also in this case, some numerical simplifications have been used to keep the

*Ph.D. Candidate; h.shahzad@tudelft.nl (Corresponding Author).

†Professor, Delft University of Technology, Kluyverweg 2, 2629 HS Delft, The Netherlands.

‡Assistant Professor, Gran Sasso Science Institute, L'Aquila, 67100 Abruzzo, Italy.

computational cost acceptable, such as simulating a single line of resonators in the spanwise direction, and a limited number or resonators in the streamwise direction. The mesh resolution of that study might have been too coarse, according to the authors, who reported large discrepancies on the acoustic resistance between simulations and experiments, and suggested that a finer mesh might be necessary to reduce this disparity. Despite the simplifying modeling assumptions, these numerical simulations have helped shape our understanding of acoustic liners, and although the aerodynamic aspect of acoustic liners is still relatively obscure, their acoustic behavior is now relatively better understood.

To the best of our knowledge, none of the available experimental studies [10–12] performed direct drag measurements, but some studies estimated the added drag from the pressure drop [10,12]. Our group has recently performed unprecedented direct numerical simulation (DNS) of channel flow over pore-resolved acoustic liners [13–15] and estimated that acoustic liners are responsible for a 70% drag increase per plane area in operating conditions. Additionally, we also identified the nonlinear permeability of the facesheet as relevant length scale to characterize the aerodynamic effect of these surfaces.

The aerodynamic impact of acoustic liners may vary depending upon the operating conditions. Not only are acoustic liners subject to turbulent grazing flow, but also to high-amplitude acoustic forcing. The coupled interaction of turbulent grazing flow and acoustic forcing may lead to complex interactions inside the orifice. It is well known that grazing flow alters the acoustic performance of acoustic liners, evidenced by the works of Malmary et al. [16], Jing et al. [17], Eldredge and Dowling [18], and Zhang and Cheng [19], among others, and the acoustic performance itself scales with the boundary-layer displacement thickness [20–22]. So, although it is relatively well understood that acoustic performance is altered by the boundary layer, the converse is not fully clear. Numerical simulations of resolved liner geometries with incoming acoustic noise are limited. Relevant studies include the one by Zhang and Bodony [5], Avallone et al. [4], and Avallone and Casalino [23], all with a single resonator, whereas the most recent work by Pereira et al. [9] simulated an array of resonators. Zhang and Bodony [5] described how acoustic forcing leads to high wall-normal velocity fluctuations that may dwarf the turbulent fluctuations if the amplitude of the forcing is high enough. They noted a drag increase of 25% in the presence of 140-dB sound waves and a drag increase of approximately 100% in the presence of 160-dB sound waves, compared to 4.2% without sound waves, hinting at a significant influence of acoustic forcing aerodynamic performance. However, the results are in contrast with the experiments of Howerton and Jones [10], who saw virtually no influence of 140-dB acoustic waves on the added drag. These discrepancies are common in studies investigating the aerodynamic influence of acoustic liners, because of the use of simplifying approximations for the porous surface. Whereas there are discrepancies on the effect of incoming acoustic waves on drag, the opposite is less debated and more than one study reported differences in acoustic impedance with and without grazing flow [9,17,24].

Acoustic liners belong to the class of porous surfaces, which are far less understood than canonical rough surfaces. An important topic of practical relevance that falls in this category is the response of a turbulent boundary layer to a step change in wall permeability. For canonical roughness, the literature on this topic is extensive [25–28], as changes in surface roughness are commonplace. It is well known that the onset of a rough wall on an incoming smooth-wall boundary layer (or vice versa) leads to an extended region where the flow has not yet adapted to the discontinuous surface change. The influence of the new surface conditions is initially constrained to the region in the immediate vicinity of the surface, and extends slowly upward until the entire boundary layer is influenced by, but is not necessarily in equilibrium with, the new surface geometry. The internal boundary layer (IBL) in the flow demarcates the wall-normal extent to which the influence of the new surface extends; see Fig. 1. The height of the IBL grows until it extends to the edge of the boundary layer and the growth is often correlated to
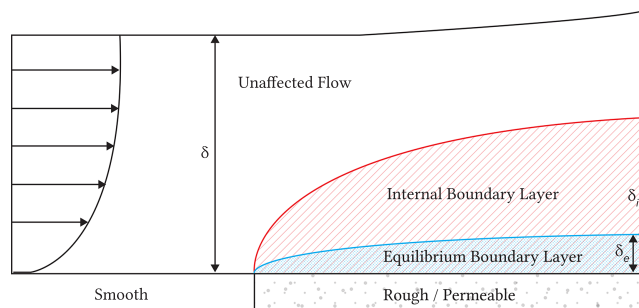

Fig. 1 Schematic depicting the development of the internal boundary layer after a smooth-to-rough transition. The red line depicts the height of the internal boundary layer and its development in the streamwise direction and the blue line indicates the extent of the equilibrium boundary layer.

the downstream distance from the smooth-to-rough transition point in the form, $\delta_I \propto (x - x_t)^\theta$, where θ is the growth rate exponent, δ_I is the height of the IBL, and $(x - x_t)$ is the streamwise distance downstream of the smooth-to-rough transition point.

The seminal work of Elliott [25] identified that, following a step change in surface roughness, two equilibrium (logarithmic) layers coexist in the mean streamwise velocity profile, and identified the height of the IBL as the intersection of the two log laws. Alternative definitions [26,29] of the height of the IBL employ similar techniques to identify changes in the mean streamwise velocity or the streamwise Reynolds stress, and depending upon the exact definition used, the resulting growth rate θ may differ significantly [27]. For instance, Efros and Krogstad [29] reported a growth rate of $\theta \approx 0.7$, compared to $\theta \approx 0.8$ of Elliott [25] and $\theta \approx 0.33$ of Cheng and Castro [26], with the difference in growth rate primarily down to the different definitions employed [27]. Regardless of the definition used to calculate the height of the IBL and the geometry considered, the IBL growth rates for canonical surfaces have generally ranged between $\theta \approx 0.2$ and 0.8.

Much less is known about the development of the IBL over porous surfaces and it is not clear whether permeable surfaces behave similarly and whether the growth rate of the IBL over permeable surfaces follows similar trends as rough canonical surfaces. Efstathiou and Luhar [30] observed that the IBL over their porous surface grew rapidly to the edge of the boundary layer within 10δ, where δ is the local boundary-layer thickness, in a similar manner to canonical rough surfaces. However, the exact growth rates of the IBL were not measured and the discussion was limited to a qualitative comparison with canonical rough surfaces.

The present paper extends recent work on acoustic liners, by studying a more realistic numerical setup than ever done before, by performing DNS of a turbulent boundary layer over fully resolved acoustic liner arrays. The aim of this work is twofold:

1) We aim to validate our previous findings [14], obtained using a biperiodic channel flow configuration, using the more realistic case of a developing boundary layer, which also allows us to introduce acoustic waves and assess their influence on the flow.

2) We study the adjustment of the flow to a step change in permeability, which is common in engineering applications.

The considered setup and methodology are detailed in the following section. Results for the turbulent flow without external acoustic excitation are presented in Sec. III. The effect of 150-dB sound waves is discussed in Sec. IV, followed by conclusions in Sec. V.

II. Methodology

A. Boundary-Layer Setup

We perform DNS of a turbulent boundary layer over acoustic liners using the flow solver STREAmS [31,32]. The compressible Navier–Stokes equations are discretized using a finite difference method where convective derivatives are approximated with a sixth-order locally conservative central scheme, and a second-order locally conservative discretization is used for the viscous

terms. Time advancements are performed using a third-order Runge–Kutta scheme. Additional details on the solver are available in the reference publication [32]. The simulation is performed in a rectangular box of size $L_x \times L_y \times L_z = 115\delta_0 \times (15\delta_0 + k) \times 5\delta_0$, where δ_0 is the inflow boundary-layer thickness, k is the depth of the acoustic liner, and x, y, and z are the streamwise, wall-normal, and spanwise directions, respectively. We note that the boundary-layer thickness grows in the streamwise direction, thus the effective box dimensions become smaller, compared to the local boundary-layer thickness δ. At the outflow, the spanwise size of our domain approaches $L_z \approx 2\delta$. This domain size may seem small in absolute terms, however, similar and even smaller spanwise domains have been used previously to aid parametric analysis of rough-wall turbulent flows [33–38], including our previous study in turbulent plane channel flow, where we used $L_z \approx 1.5\delta$ [14]. For rough-wall turbulent flow simulations, smaller computational box sizes are accepted for two reasons:

1) They relax the higher computational cost that is required to resolve the roughness.

2) The main interest when studying roughness is in the log layer, which is not affected by small box dimensions, as demonstrated by Chung et al. [35].

The freestream Mach number is $M_\infty = u_\infty/c_\infty = 0.3$, where u_∞ is the freestream velocity and c_∞ is the speed of sound based on freestream conditions, and the friction Reynolds number is $Re_\tau = \delta/\delta_v \approx 850$–2600. The domain consists of an initial smooth-wall region of streamwise length $L_{x,s} = 45\delta_0$, followed by an acoustic liner array that extends from $x = 45\delta_0$ to the end of the domain, $x = 115\delta_0$. The equations are discretized on a Cartesian grid with a mesh size $N_x \times N_y \times N_z = 21504 \times 672 \times 1120$. The mesh spacing is constant in the spanwise direction and points are clustered in the wall-normal direction at the liner facesheet and coarsened toward the backplate and the freestream. The mesh points are slightly clustered close to the transition point between the smooth wall and the liner and have a constant spacing over the liner. The orifice geometry is resolved by 24 points in the streamwise and spanwise directions. This mesh resolution has been verified in a previous work, where we carried out a mesh refinement study showing that this number of point yields has grid-converged results [14]. Details of the simulation are summarized in Table 1. A characteristic nonreflecting boundary condition is used at the top boundary. At the inflow and the outflow, the nonreflective condition is augmented with relaxation [39] to impose a realistic turbulent profile at the inflow, and the pressure value at the outflow. At the inflow, we impose the mean streamwise velocity obtained from the composite profile of Musker [40], with superposed turbulent velocity fluctuations from a recycling–rescaling procedure [41,42]. The recycling plane is located at $x/\delta_0 = 40$, at a distance $5\delta_0$ upstream of the point of transition from the smooth wall to the liner. Periodic boundary conditions are used in the spanwise direction. The geometry, consisting of the smooth wall and the liner, is resolved using a ghost-point immersed boundary method [43] enforcing a nonslip adiabatic boundary condition.

The geometry of the acoustic liners is chosen to match as closely as possible a realistic acoustic liner in operating conditions. Our cavity geometry has a square cross section with a side length $\lambda = 0.5\delta_0$ and depth $k = 2.0\delta_0$. Each cavity has nine orifices with a diameter corresponding to a porosity of $\sigma \approx 0.322$. The geometry of the facesheet is similar to the one studied in our channel flow simulations [14] at $\sigma \approx 0.322$ and thickness-to- diameter ratio

$t/d = 1$. The domain consists of a total of 140×10 acoustic liner cavities in the streamwise and spanwise directions.

Quantities that are nondimensionalised by δ_v and u_τ are denoted by the "+" superscript. Favre-averaged variables are indicated by $(\tilde{\cdot})$, whereas Reynolds-averaged variables are indicated by $(\bar{\cdot})$. For instance, $\tau_{ij} = \overline{\rho\, \widetilde{u_i'' u_j''}}$, indicates the Reynolds stress tensor, where the double prime symbol indicates fluctuations with respect to the Favre average. Statistics are averaged in the spanwise direction and in time. Statistics are also averaged in the streamwise direction over a single cavity representing a streamwise extent of $\approx 0.5\delta_0$, to ensure better statistical convergence. Statistics are collected every $\Delta t \approx 0.3\delta_0/u_\infty$ for a total time of $t_{\text{tot}} = 150\delta_0/u_\infty$. We estimated the extent of convergence by residual of the streamwise mean momentum balance,

$$\frac{\partial}{\partial x}(\bar{\rho}\tilde{u}\tilde{u}) + \frac{\partial}{\partial y}(\bar{\rho}\tilde{u}\tilde{v}) = -\frac{\partial\bar{p}}{\partial x} - \frac{\partial}{\partial y}(\overline{\rho u'v'}) + \frac{\partial}{\partial y}\left(\bar{\mu}\frac{\partial\tilde{u}}{\partial y}\right) \quad (1)$$

The residual of Eq. (1) $R(x,y)$ is integrated in the wall-normal direction,

$$\epsilon(x) = \left(\frac{1}{h}\int_0^\delta R(x,y)^2\, dy\right)^{1/2} \quad (2)$$

and we find that its maximum value nowhere exceeds $\epsilon/(\rho_w u_\tau^2/\delta_v) \approx 4 \times 10^{-3}$. This value is in line with the convergence criterion proposed by Vinuesa et al. [44] for plane channel and square duct flow.

B. Sound Waves

We perform two boundary-layer simulations L_1 and L_2 with identical setup; apart from that the latter features incoming acoustic waves. When present, acoustic waves are introduced at the outflow boundary, where the outflow pressure is relaxed toward a target value $p_o(t) = p_0 + A\cos(2\pi f_o T)$, which oscillates around the reference freestream thermodynamic pressure p_0 with amplitude A, and T is time and $f_0 = c/(2\pi)\sqrt{O_A/t'V} \approx 0.422 u_\infty/\delta_0$ is the resonance frequency of the liner. c is the speed of sound, O_A is the area of the orifices, $t' = t + 1.6\sqrt{A/\pi}$ is the thickness of the orifice corrected for the influence of the pressure field on the apparent mass of air in the orifice [5,45,46], and V is the volume of the cavity. For case L_1, no sound wave is imposed at the outflow, and the amplitude of the sound wave is set to zero. For case L_2, sound waves with a sound pressure level SPL = 150 dB are imposed at the outflow using a characteristic-based relaxation [39]. The corresponding amplitude is $A = p_r \cdot 10^{\text{SPL}/20}$, where $p_r = 20 \times 10^{-6}$ Pa is a reference pressure.

The reason for choosing a 150-dB amplitude is motivated by previous studies that used amplitudes in the range 130–150 dB. We decided to pick a value in the upper range in the attempt to maximize the effect on the turbulent boundary layer. We introduce acoustic waves at the outflow traveling upstream. This is partially motivated by our turbulent inflow generation based on a recycling/rescaling technique, which would be more cumbersome to implement with the addition of incoming noise. Introducing acoustic noise at the inflow traveling downstream would have also been a valid option, and it has been pursued by other authors [9]. It is worth noting that

Table 1 DNS parameters for the two boundary-layer cases considered, L_1 and L_2, in the absence and presence of acoustic waves. The computational domain has dimensions $L_x \times L_y \times L_z = 115\delta_0 \times 15\delta_0 + k \times 5\delta_0$ and the number of mesh points is $N_x \times N_y \times N_z = 21504 \times 672 \times 1120$. σ is the porosity (open area ratio). Re_τ and δ/δ_0 are the friction Reynolds number and the local boundary-layer thickness. Δx^+, Δy^+, and Δz^+ are the viscous-scaled mesh spacings in the streamwise, wall-normal, and spanwise directions

Case	σ	Re_τ	δ/δ_0	$\Delta x^+_{\max}$	$\Delta y^+_{\min}$	$\Delta z^+_{\max}$	$f\delta_0/u_\infty$	SPL, dB
L_1	0.322	854–2587	0.86–2.43	8.26	0.79	5.55	0	0
L_2	0.322	861–2601	0.86–2.47	8.51	0.81	5.72	0.422	150

noise directionality matters in the presence of a grazing flow [9]. We note that acoustic waves coming from the outflow are closer to the case of acoustic liners in the aircraft engine intake [22], where noise is coming from the fan and traveling upstream of the boundary layer. However, we also point out that in real conditions acoustic waves are reflected and scattered on the walls of the engine and the aircraft, thus acoustic waves come from other directions as well.

To prevent the interaction of acoustic waves with the recycling, selective frequency damping (SFD) [47,48] was used. SFD is based on control theory and adds a linear term to the Navier–Stokes to force toward a particular filtered solution, $\dot{q} = \mathcal{F}(q) - \chi(q - q_f)$, where q is the vector of conservative variables in the Navier–Stokes, q_f is the filtered solution, and χ is the control parameter. The encapsulated form of the equations [47] is used where the filtered solution is defined as $\dot{q}_f = 1/\Delta(q - \dot{q}_f)$, and Δ represents the cutoff frequency. SFD is active in the region $0 < x/\delta_0 < 70$, only above the boundary-layer height. The control parameter χ is ramped up linearly in the upstream direction from $\chi = 0$ at $x/\delta_0 = 70$ to $\chi = 0.8$ for $x/\delta_0 < 45$. The region between $x/\delta_0 = 70$ and the outflow is where we can reliably study the action of acoustic waves on acoustic liners.

III. Turbulent Boundary Layer Without Sound Waves

A. Instantaneous Flowfield

An instantaneous flow visualization of the flowfield is shown in Fig. 2, where vortices are visualized using the Q criterion. The figure shows the complex organization of the turbulent structures and the growth of the boundary layer in the streamwise direction. Additional insight on the flow can be gained by inspecting wall-parallel planes close to the wall. Figure 3 shows the streamwise and wall-normal instantaneous velocity on an $x - z$ plane over the smooth-to-liner transition region. Compared to the smooth wall, the liner leads to very high wall-normal velocity fluctuations near the surface of the facesheet; see Fig. 3b. High-velocity magnitudes tend to be concentrated around the orifices. Wall-normal velocity fluctuations have been previously observed to play an important role in altering the near-wall cycle [49–51], and have been proposed as the mechanism that leads to the drag increase over acoustic liners by Wilkinson [52] and Shahzad et al. [14]. Compared to the smooth wall, the streamwise velocity contours are also significantly altered; see Fig. 3a. High-speed and low-speed streaks, typical of

near-wall turbulence, are perturbed by the significant wall-normal velocity fluctuations at the wall and, thus, break down over the liner. Immediately after the smooth-to-porous transition, between $(x - x_t)/\delta_0 \approx 2$ and $(x - x_t)/\delta_0 \approx 5$, there exists a small region where the flow over the liner appears marginally distinct from the flow farther downstream. The wall-parallel planes show a spanwise coherent flow organization, resembling Kelvin–Helmholtz-like structures, which have generally been previously observed over porous surfaces [6,53] and riblets [54].

The high wall-normal velocity fluctuations induced by the liner are due to the interaction of the flow above and below the facesheet, evidence of which can be seen in Fig. 4a, showing wall-normal velocity and pressure fluctuations in an $x - y$ plane. A jetlike flow is observed penetrating into the cavities, indicating high inertial effects inside the liner. Shahzad et al. [14] noted that this jetlike flow is a result of pressure fluctuations redistributing energy into wall-normal velocity fluctuations. Figure 4b shows contours of the pressure fluctuations in an $x - y$ plane. In a similar fashion to the wall-normal velocity fluctuations, pressure fluctuations significantly increase as the flow passes from the smooth wall to the liner, particularly close to the wall. High-pressure regions are observed closer to the downstream edge of the orifice, hinting at an increase in pressure drag over acoustic liners. Shahzad et al. [14] noted that pressure drag significantly increases over a liner, reaching nearly 50% of the total drag of the surface in their channel-flow simulations. We also note that the cavity and orifice pressure seem to respond to the large-scale structures in the boundary layer.

B. The Internal Boundary Layer

We continue our discussion by investigating how the flow reacts to the step change in permeability. To calculate the height of the IBL, we use the method proposed by Cheng and Castro [26], who used the point where the downstream velocity is 99% of the upstream velocity before the surface transition at the same wall-normal location and reported a growth rate of the IBL thickness $\delta_I \propto (x - x_t)^{0.33}$. Here, the method proposed by Cheng and Castro [26] is used because it is found to be more robust than the one by Elliott [25], which requires the identification of two logarithmic regions in the mean velocity profile, leading to a larger uncertainty for the present simulations.

Figure 5a shows a graphical representation of the method by Cheng and Castro [26] to calculate the IBL height. The heights of
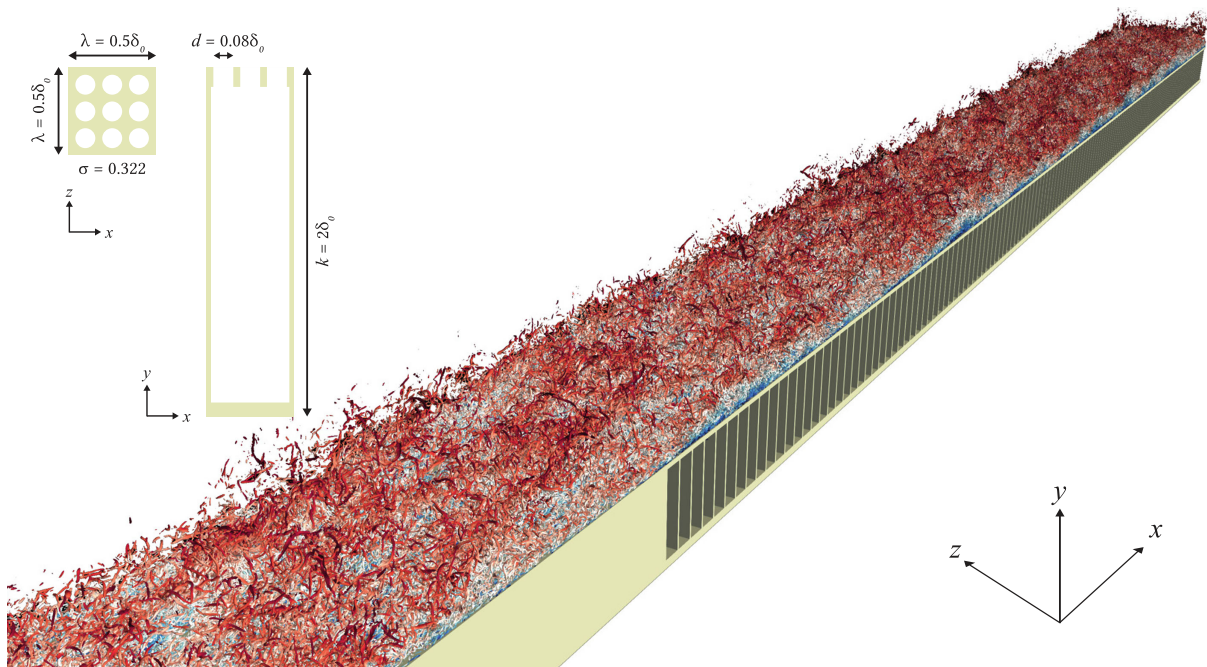

Fig. 2 Instantaneous flowfield of the boundary-layer simulation. Orifice configurations within a single cavity are also shown at the top left. Vortical structures are visualized using the Q-criterion, colored by the streamwise velocity.
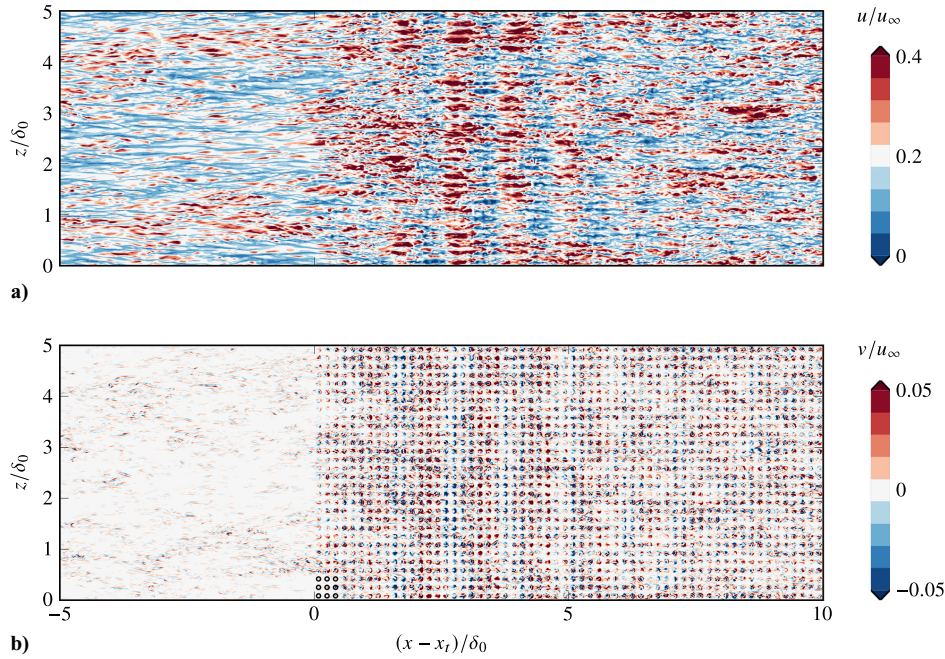
Fig. 3   a) Instantaneous streamwise velocity, and b) wall-normal velocity fluctuations in a wall parallel plane at $y/\delta_0 = 0.005$. The position of the orifices is shown for a single cavity at the smooth-to-porous transition. x_t represents the streamwise location of the smooth-to-porous transition point.
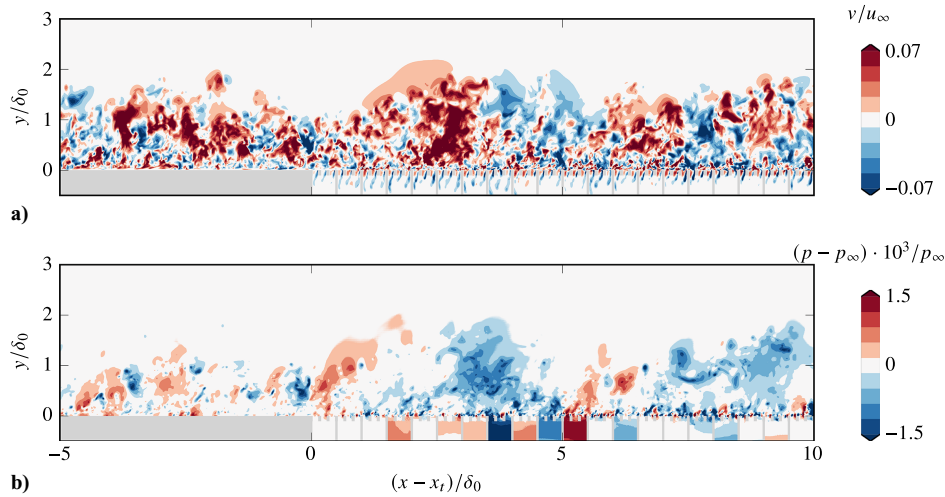

Fig. 4   a) Instantaneous wall-normal velocity, and b) pressure fluctuations in an $x-y$ plane. x_t represents the streamwise location of the smooth-to-porous transition point.
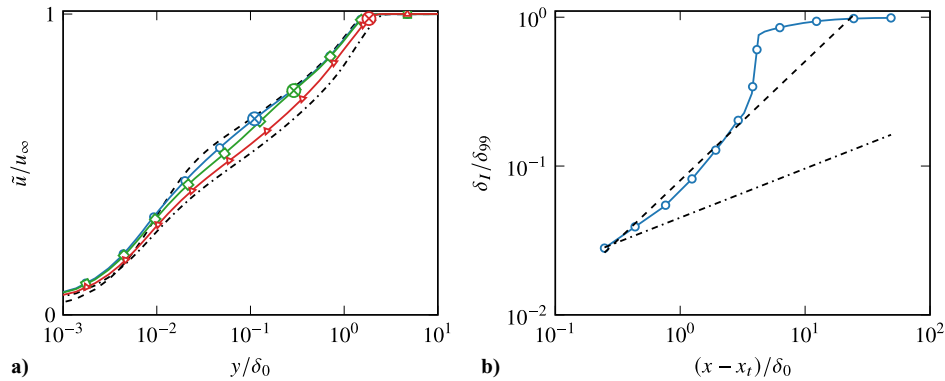

Fig. 5   Evaluation of the internal boundary layer using the streamwise velocity as in Cheng and Castro [26]. In a), the solid line with symbols represents the streamwise velocity downstream of the smooth-to-porous transition point at $(x - x_t)/\delta_0 \approx 1.25$ (circles), 5 (squares), and 25 (triangles), the dashed line represents the upstream velocity profile over the smooth wall, and the dashed-dotted line represents the liner velocity profile, significantly downstream of the transition point. The red cross is used to identify the wall-normal location of the internal boundary layer. In b), the growth of the internal boundary layer in the streamwise direction (circles) is compared to growth rate suggested by Elliott [25] (dashed line: $\delta_I \propto (x - x_t)^{0.8}$) and Cheng and Castro [26] (dash-dotted line: $\delta_I \propto (x - x_t)^{0.33}$).

the IBL, at three different streamwise locations, are marked with large encircled crosses, indicating the point where the velocity at the three streamwise locations is 99% of the upstream velocity at the same wall-normal location. The growth of the IBL is shown in Fig. 5b, along with the growth rates suggested by Cheng and Castro [26] and Elliott [25]. The adjustment of the streamwise velocity profile is quick and the height of the IBL is approximately equal to the local boundary-layer thickness at a distance $10\delta_0$ downstream of the smooth-liner transition, similar to the permeable surfaces considered by Efstathiou and Luhar [30]. Compared to the growth rate suggested by Cheng and Castro [26], the present IBL grows at a quicker pace. The growth rate of the IBL matches the growth rate suggested by Elliott [25] in the immediate vicinity of the transition point. However, the growth rate for the acoustic liner is not constant and increases downstream, recovering faster than what was suggested by Elliott [25]. Figure 6 shows the IBL location superimposed on top of the wall-normal gradient of the mean streamwise velocity. One could argue that the development of the Kelvin–Helmholtz-like structures cause more intense mixing and momentum transfer, leading to a quicker adjustment of the mean streamwise velocity. The recovery of the streamwise velocity is, therefore, faster over an acoustic liner than over canonical roughness.

However, the adjustment of the streamwise Reynolds stress is much slower. Efros and Krogstad [29] used profiles of the streamwise Reynolds stress to estimate the thickness of the IBL, as represented in Figs. 7a–7c, where the IBL thickness is estimated to be at the intersection between the two linear regions in the streamwise Reynolds stress. Figure 7d shows the height of the IBL, estimated with this method, as a function of distance downstream of the smooth-liner transition. The growth initially matches that suggested by Efros and Krogstad [29] of approximately $\delta_I \propto (x - x_t)^{0.7}$, but deviations are visible farther downstream, most probably associated with the large uncertainty in accurately fitting two linear regions in the streamwise Reynolds stress. Therefore, we believe we can assume that the recovery of streamwise Reynolds stress follows similar trends as canonical roughness. If the growth rate suggested by Efros and Krogstad [29] is extrapolated, the IBL approaches approximately 90% of the local boundary-layer thickness toward the end of the domain, therefore, it can be safely assumed that the Reynolds stresses do not reach equilibrium in the present simulations.

C. Mean Flow and Skin Friction

Figure 8 shows the friction coefficient, C_f, and the friction Reynolds number, Re_τ, as a function of the Reynolds number based on the streamwise distance from the virtual leading edge. Both the friction Reynolds number and the friction coefficient tend to overshoot at the smooth-to-porous transition as the flow tries to adjust itself to the new flow conditions. Away from the transition location, the overshoot in the friction coefficient decreases, but drag remains higher than for the smooth wall.

The added drag is also visible in the mean streamwise velocity over the liner, shown in Fig. 9a. Velocity profiles past the smooth-to-liner transition point show a downward shift as compared to the smooth wall. This downward shift, defined as $\Delta U^+ = \tilde{u}_s^+ - \tilde{u}^+$, is where $\tilde{u}_s^+$ and $\tilde{u}^+$ are the streamwise velocities over the smooth wall, and the acoustic liner in the logarithmic layer, respectively, is a measure of drag increase. Furthermore, differences between the

smooth wall and liner velocity profiles are limited to the near-wall region, and the velocity profiles are essentially parallel in the outer layer, indicating that Townsend's outer layer similarity hypothesis holds for the streamwise velocity. The streamwise velocity profiles over the liner exhibit a nearly constant ΔU^+ (see Fig. 10a) apart from a small region near the smooth-to-liner transition point.

Differences between the smooth wall and the liner are visible in the Reynolds stresses, $\tau_{ij} = \overline{\rho} \, \widetilde{u_i'' u_j''}$, shown in Fig. 9b. We compare the results of the liner case with the smooth-wall cases of Eitel-Amor et al. [56] at approximately matching friction Reynolds number. Deviations from the smooth-wall Reynolds stresses are visible close to the wall. Irrespective of the velocity component, nonzero Reynolds stresses exist near the wall for the liner, which enhance momentum transfer and contribute to the added drag. The nonzero wall-normal velocity fluctuations near the wall, also evident in the instantaneous flow in Fig. 3b, are responsible for the breakdown of the classical near-wall turbulence cycle and a reduction in the streamwise Reynolds stress peak. The peak streamwise Reynolds stress decreases over the acoustic liner and the peak spanwise and wall-normal velocity fluctuations increase with respect to the smooth wall, in contrast to the channel flow simulations of Shahzad et al. [14], for which we observed only an increase in the peak of the spanwise velocity fluctuations. Differences can be observed in the outer layer because the Reynolds stresses are not in equilibrium yet.

D. Acoustic Liners as a Permeable Substrate

Recently, we have analyzed several candidate length scales for acoustic liners [14] and observed that the inverse of the viscous-scaled nonlinear (Forchheimer) permeability, $1/\alpha^+$, is the relevant length scale for acoustic liners. We attribute this to the very high inertial effects that may be observed inside the orifices. The present boundary-layer results also support this finding, as shown by Fig. 10b, where we report ΔU^+ as a function of the viscous-scaled inverse of the Forchheimer coefficient, which exactly follows the trend observed in the channel flow simulations, and matches remarkably well the correlation proposed for ΔU^+ in the seminal work of Colebrook [58]. The good match with our channel flow data is despite a different cavity depth of $k/\delta = 0.822–1.267$ for our boundary-layer simulation as compared to $k/\delta = 0.5$ for the channel flow simulations, where δ is the local boundary-layer thickness and the channel half width, respectively. We also note that channel flow simulations [14] were performed in a smaller box with spanwise size $L_z = 0.5\delta$, but this does not affect the Hama roughness function, as anticipated by Chung et al. [35]. The cavity depth, therefore, does not play a significant role in determining liner behavior in the absence of sound waves.

Acoustic liner drag not being affected by cavity depth is in line with previous observations by Howerton and Jones [10], who noted that, in the absence of acoustic excitation, liner drag is not changed by changing the cavity depth. Therefore, the aerodynamic properties of acoustic liners are determined by the permeability of the facesheet and the orifice geometry. The latter has also been recently shown by Shahzad et al. [15].

E. Spectral Densities

Figure 11 shows the premultiplied spanwise spectral densities of the streamwise, $\kappa_z^+ E_{u,z}/u_\tau^2$, and wall-normal velocity, $\kappa_z^+ E_{v,z}/u_\tau^2$,
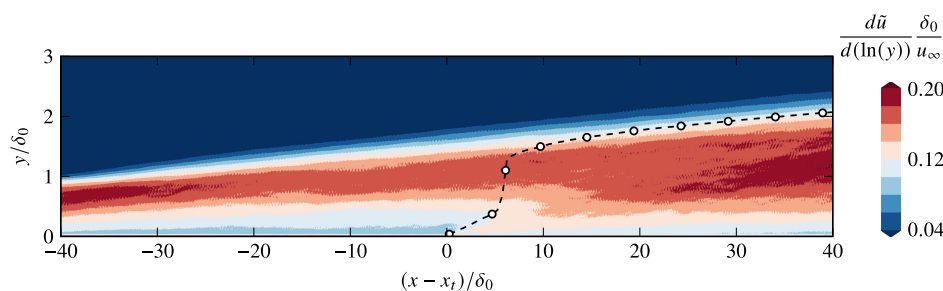

Fig. 6 Wall-normal gradient of the streamwise velocity. The markers indicate the location of the IBL.
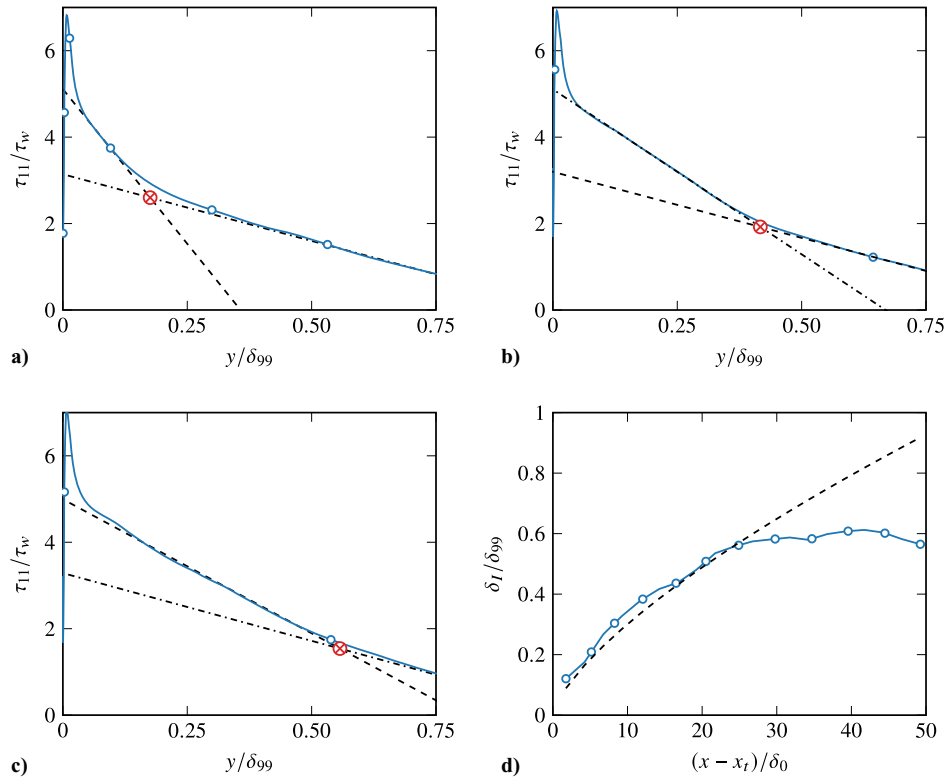
Fig. 7 Evaluation of the internal boundary layer using the streamwise Reynolds stress as proposed by Efros and Krogstad [29]. In a)–c), the solid line with circles represents the streamwise Reynolds stress downstream of the smooth-to-porous transition point at a) $(x - x_t)/\delta_0 \approx 4$, b) $(x - x_t)/\delta_0 \approx 15$, and c) $(x - x_t)/\delta_0 \approx 25$, and the dashed and dashed-dotted lines are linear fits to the two straight line segments of the streamwise Reynolds stress. The intersection of the two lines shown by the red cross is the wall-normal location of the internal boundary layer. In d), the growth of the internal boundary layer in the streamwise direction (circles) is compared to the growth rate suggested by Efros and Krogstad [29] (dashed line: $\delta_I \propto (x - x_t)^{0.7}$).
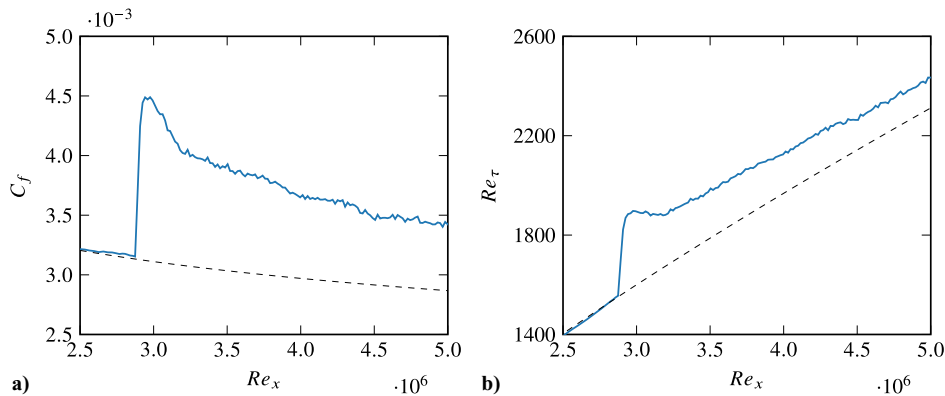

Fig. 8 Variation of the a) friction Reynolds number, and b) the skin-friction coefficient for the boundary-layer simulation with the distance from the smooth-to-porous transition point. Solid lines show the boundary-layer simulation results and the dashed lines show smooth wall Re_τ and C_f, approximated using $C_f = (2\log_{10}(Re_x) - 0.65)^{-2.3}$ [55], where a virtual origin is used to calculate Re_x by matching DNS results for using skin-friction data at the inflow.

components as a function of the wall-normal distance from the virtual origin and the spanwise wavelength λ_z, for flow cases $L\text{-}L_{32}$, $L\text{-}M_{32}$, and $L\text{-}H_{32}$. The spectral densities are defined such that

$$\widetilde{f''^2} = \int_{-\infty}^{+\infty} E_f(\kappa_z)\, d\kappa_z \qquad (3)$$

where κ_z is the spanwise wavenumber. The instantaneous flow showed significant differences between the smooth-wall and the liner, indicating a difference in the organization of turbulence. Spectral analysis can provide further insight and a more quantitative view into how the acoustic liner influences the turbulent flow organization. Figure 11 shows the premultiplied spectral densities

of the streamwise velocity, wall-normal velocity, and pressure as a function of the viscous-scaled wall-normal distance for two different streamwise stations in the domain: before the smooth-liner transition and downstream of the point of transition.

Differences between the smooth-wall spectral densities and liner spectral densities are clearly visible. Unlike the broadband nature of the smooth-wall streamwise spectral density, the streamwise spectral densities for the liner show a tonal concentration of energy at wavelengths close to the orifice spacing (dashed black). These wavelengths near the orifice spacing contain a significant proportion of the energy, and the near-wall peak at $y^+ \approx 10\text{–}30$ is lower than for the smooth wall. This is consistent with the disruption of the near-wall cycle observed in the instantaneous velocity field in Fig. 3. A similar trend is observed for the pressure fluctuations. Pressure
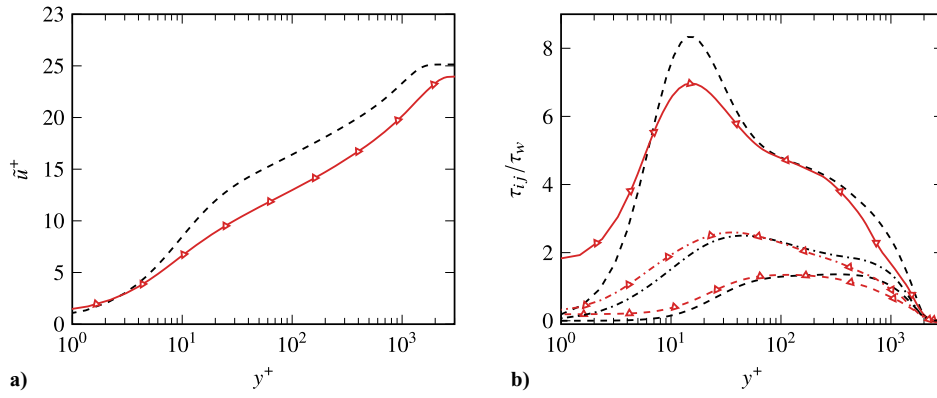
Fig. 9 Mean streamwise velocity a) as a function of the wall-normal coordinate. Different line types represent different streamwise locations in panel a): triangles ($(x - x_t)/\delta_0 \approx 45$) and dashed line ($(x - x_t)/\delta_0 \approx -5$). Streamwise (solid), wall-normal (dashed), and spanwise (dashed-dotted) Reynolds stresses b) over the acoustic liner (lines with triangles) compared to the smooth wall data of Eitel-Amor et al. [56] (lines) at friction Reynolds number, $Re_\tau \approx 1940$.
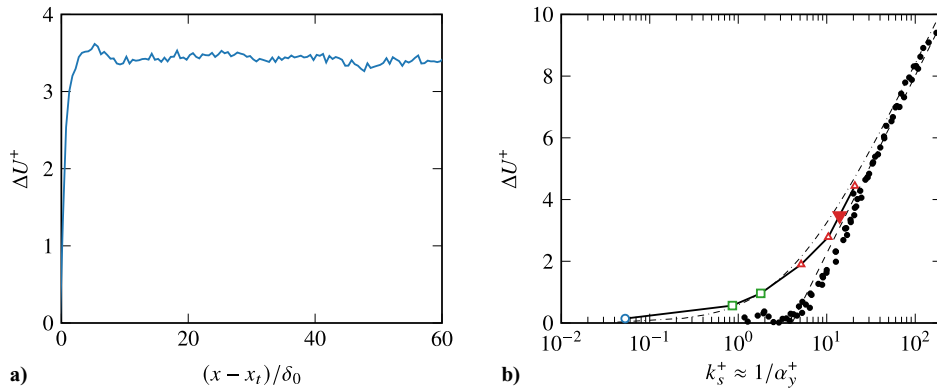

Fig. 10 ΔU^+ as a) a function of the distance from the transition point, and b) as a function of the viscous-scaled inverse of the Forchheimer coefficient. The filled inverted triangle represents ΔU^+ of the current simulation, whereas the empty symbols represent data of channel flow simulations [14]. Filled circles are Nikuradse's data [57] for sand-grain roughness, the dashed line shows the fully rough asymptote, and the dashed-dotted line represents data for Colebrook-type roughness [58].
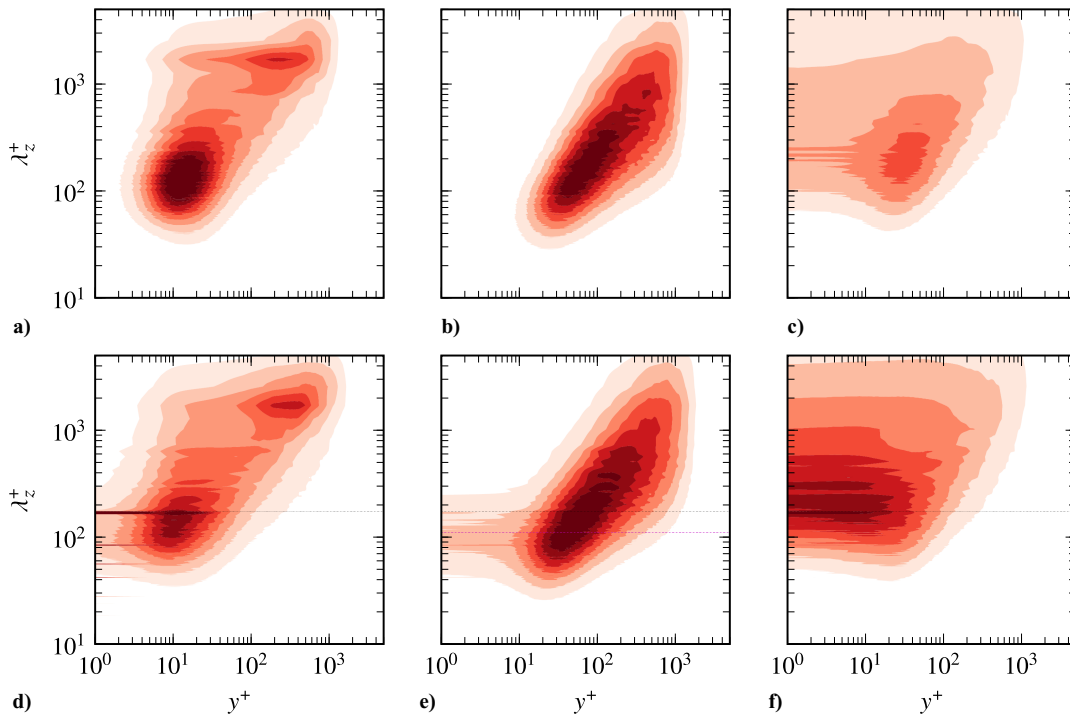

Fig. 11 Premultiplied streamwise, $\kappa_z^+ E_{u,z}/u_\tau^2$ [a), d)], wall-normal, $\kappa_z^+ E_{v,z}/u_\tau^2$ [b), e)], and pressure, $\kappa_z^+ E_{p,z}/\tau_w^2$ [c), f)] spectral densities as a function of the viscous-scaled wall-normal distance for smooth wall ($(x - x_t)/\delta_0 \approx -5$ [a)–c)]) and liner ($(x - x_t)/\delta_0 \approx 45.25$ [d)–f)]). λ_z^+ is the viscous-scaled spanwise wavelength and κ_z is the spanwise wave number.

fluctuations are significantly enhanced downstream of the point of transition. This was easily observed in contours of the pressure fluctuations in an $x - y$ plane, shown in Fig. 4b, and can also be seen in the spectral densities. The wavelength of the maximum pressure fluctuations shifts closer to the orifice spacing. Furthermore, whereas the energy in the pressure fluctuations over the smooth wall is concentrated away from the wall, energy in pressure fluctuations resides primarily near the wall for the case of the acoustic liner. Figure 4 shows how high-pressure fluctuations exist near the wall, toward the downstream edge of the orifices. The trend of the wall-normal velocity fluctuations, although similar to the streamwise velocity and pressure, have more energy concentrated at wavelengths smaller than the orifice spacing. Most of the energy is concentrated at wavelengths more comparable to the orifice diameter.

The spectral densities have important differences and similarities with the work of Shahzad et al. [14], who reported an influence of acoustic liners on the inner–outer scale interaction in the turbulent flow. They noted that the footprint of the larger structures on the smaller scales closer to the wall increased. There is no clear evidence of any such behavior in the current results. The difference could be due to the small domain size used in the channel flow simulations of Shahzad et al. [14], which arguably has some effect on the dynamics of the large-scale structures.

IV. Effect of High-Amplitude Sound Waves

Figures 12a–12f show the instantaneous flow over an acoustic liner that is subjected to incoming acoustic waves. The acoustic

waves have maximum intensity at the outflow and they are progressively damped, at least in the liner vicinity, as they travel upstream. The action of the selective frequency damping is also visible starting at $(x - x_t)/\delta_0 \approx 10$, quenching the acoustic waves on the smooth wall, before they reach the recycling station used to generate the inflow turbulent fluctuations. In addition to the fluctuations inside the orifice and cavity that result from the turbulent boundary layer, the acoustic wave leads to pressure fluctuations inside the cavity, particularly evident in the cavities closest to the outflow where the acoustic waves are introduced. Farther upstream, however, the flow below the surface of the facesheet, in particular, and the boundary layer, in general, appears to be relatively unaffected by the grazing sound wave, evidenced by the wall-normal velocity fluctuations shown in Fig. 12c bearing similarity to the turbulent grazing flow without sound waves. In a very similar fashion to flow in the absence of acoustic waves, and the results of Shahzad et al. [14], an asymmetric distribution of the flow inside the orifice is observed with high wall-normal velocity fluctuations primarily at the downstream edge of the orifice, superimposed on top of the vortex that resides within the orifice due to the grazing turbulent flow, possibly hinting at a more subdued reaction to the acoustic waves as compared to the turbulent grazing flow.

Zhang and Bodony [5] showed how the asymmetric flow inside the orifice becomes more symmetric due to the action of acoustic waves, and noted a significant influence of the acoustic liner on the drag if the acoustic fluctuations were higher than or of a comparable magnitude as the turbulent fluctuations, that is, at high sound pressure level (SPL). Figure 12g shows the SPL of the pressure
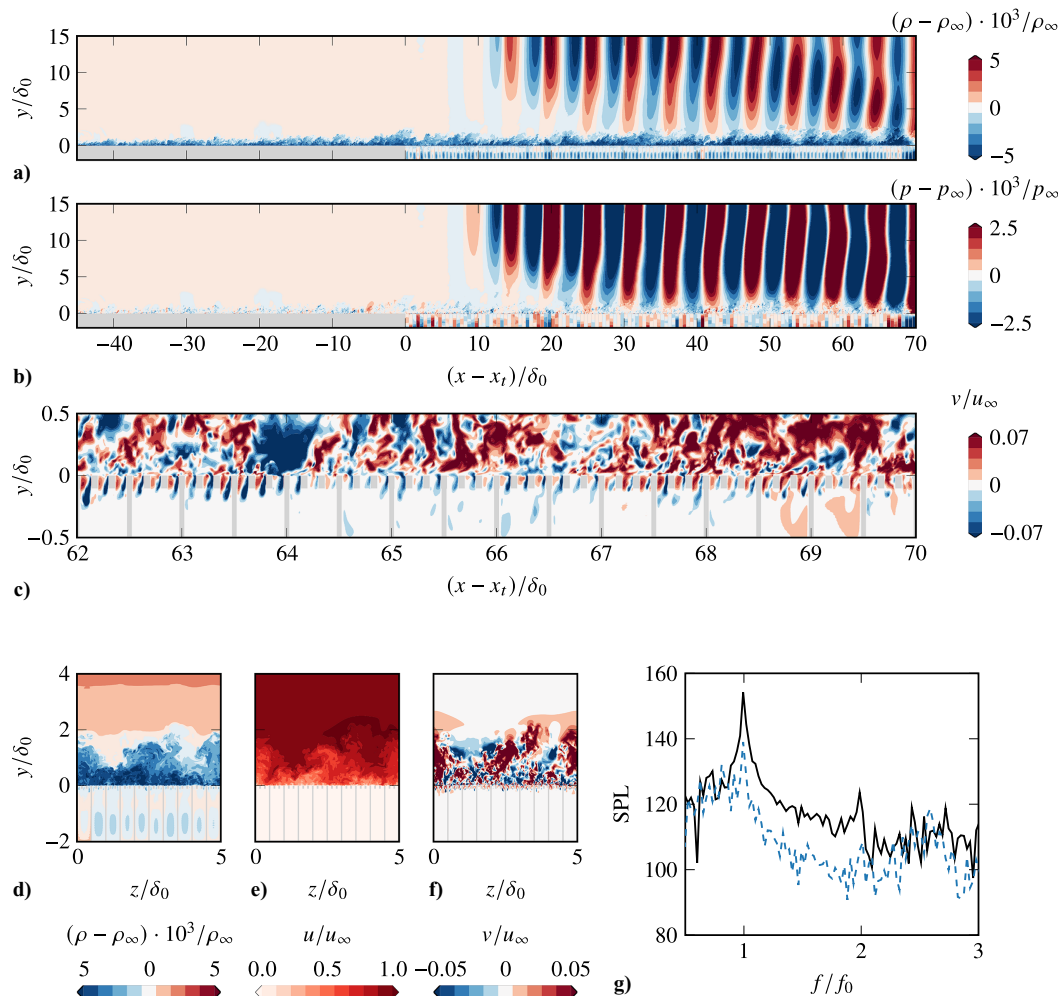

Fig. 12 a) Instantaneous density, b) pressure, and c) wall-normal velocity fields in a longitudinal plane, and d) instantaneous density, e) streamwise velocity, and f) wall-normal velocity in a cross-stream plane for acoustic liners interacting with grazing flow and acoustic forcing. The sound pressure level at the bottom of a cavity as a function of the frequency is shown in g), where the solid line is for the first cavity upstream from the outflow at $(x - x_t)/\delta_0 = 69.75$ and the dashed line is for a cavity slightly farther upstream at $(x - x_t)/\delta_0 = 67.25$.
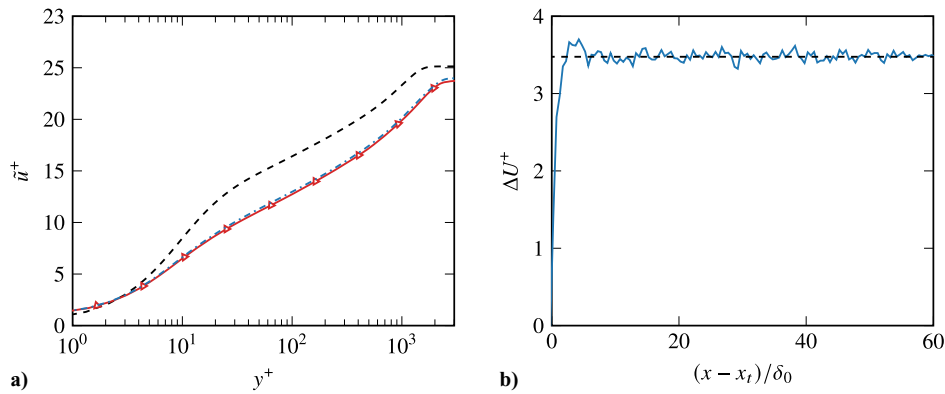
Fig. 13 a) Mean streamwise velocity for case L_2 as a function of the wall-normal coordinate. Different line types represent different streamwise locations in panel a): triangles ($(x - x_t)/\delta_0 \approx 45$) and dashed line ($(x - x_t)/\delta_0 \approx -5$). b) ΔU^+ as a function of the distance from the transition point for case L_2. The dash-dotted line in a) shows the streamwise velocity for case L_1 at the same streamwise location. The dashed line in b) shows the average ΔU^+ in the absence of acoustic waves.

fluctuations at the cavity bottom as a function of the frequency at two different streamwise locations: the middle of the first cavity upstream of the outflow at $(x - x_t)/\delta_0 = 69.75$ and farther upstream at $(x - x_t)/\delta_0 = 67.25$. The cavity closest to the outflow, where we introduce a 150-dB acoustic wave, experiences high-pressure fluctuations at the frequency corresponding to the resonance frequency and its harmonics. However, fluctuations at these frequencies decrease rapidly in the upstream direction. Already, cavities only slightly upstream have significantly decreased energy contained in this frequency band. As we move further upstream, the pressure fluctuations are more broadband in nature and the tonal peak is indistinguishable. The rapid decrease in acoustic fluctuations in the cavity, and by extension, in the region near the wall, is primarily due to the acoustic liners. The frequency of the acoustic wave is tuned to the acoustic liner resonance frequency and there is significant dissipation of energy in the region close to the wall. Acoustic liners farther upstream do not experience the high acoustic fluctuations.

As a result, the aerodynamic performance of acoustic liners appears to be largely independent of the acoustic forcing. Figure 13 shows the streamwise velocity and the Hama roughness function in the domain for the case with acoustic forcing. We note that the ΔU^+ is almost the same as in the absence of acoustic waves (dashed line). This is in line with what was observed in experiments of acoustic liners in the Grazing Flow Impedance Tube by Howerton and Jones [10], who observed no change in drag due to acoustic fluctuations. In contrast, Zhang and Bodony [5] saw a marked increase in drag as the SPL of the acoustic waves was increased in their simulations. Differences with Zhang and Bodony [5] can be explained by the manner in which the acoustic wave was introduced. We introduce a grazing acoustic wave and the region near the wall dissipates the acoustic fluctuations; Zhang and Bodony [5] introduced acoustic fluctuations from the top freestream boundary, and the liners were constantly subjected to high-SPL acoustic fluctuations.

V.   Conclusions

We performed unprecedented direct numerical simulation (DNS) of a turbulent boundary layer over a permeable surface that closely resembles acoustic liners used on the inside of aircraft engines for noise attenuation. Our work represents the first-ever fully resolved DNS of a turbulent acoustic liner flow. In a broader sense, our work adds to the body of literature on turbulent flows interacting with permeable surfaces. The present boundary-layer simulation confirms the main findings of our channel flow simulations with fully resolved acoustic liner geometries: acoustic liners lead to an increase in drag very well as compared to the smooth wall and the added drag scales with the inverse of the Forchheimer permeability coefficient. Our simulation, therefore, provides supporting evidence for acoustic liners behaving as a permeable substrate and evidence of a fully rough

regime for such permeable surfaces, in similar fashion to canonical rough-wall turbulent boundary layers.

However, we also find important differences with canonical rough surfaces, particularly in the return to equilibrium conditions after a smooth-to-liner transition. The internal boundary layer grows at a much higher rate as compared to canonical rough surfaces, possibly because the latter generally protrude into the flow, leading to a slower recovery. From a practical perspective, this means that one can neglect the spatial adjustment region in the estimation of the aerodynamic drag for acoustic liners. The Reynolds stresses, on the other hand, recover at approximately the same rate as that known for canonical rough surfaces.

Grazing acoustic waves were observed to not influence the aerodynamic performance of the acoustic liner. This agrees with the results reported by Howerton and Jones [10], who found the same added drag in flow cases with and without incoming acoustic waves. We believe, however, that this can, at least in part, be chalked down to the manner in which the acoustic wave is introduced. In real operating conditions, acoustic forcing is not necessarily a monochromatic planar grazing wave as we assumed, and the question of the combined influence of turbulent grazing flow and acoustic waves remains, to some extent, unanswered. Another important point is that even if noise was not influencing the aerodynamic performance, this does not imply the inverse. In fact, recent studies confirmed that grazing flow substantially alters the acoustic impedance [9]. In summary, much remains to be done to understand the interplay between acoustics and aerodynamics. Assuming that modeling the engine noise as a monochromatic acoustic wave is a valid assumption, one would need to run several simulations with different frequencies, amplitudes, and angles with respect to the liner. Considering that the simulations presented here have about 16 billion mesh points, developing such a data set remains a visionary task.

Acknowledgments

References

[1] Dacome, G., Siebols, R., and Baars, W. J., "Inner-Scaled Helmholtz Resonators with Grazing Turbulent Boundary Layer Flow," arXiv: 2308.07776 [physics], 2023.
https://doi.org/10.48550/arXiv.2308.07776

[2] Sivian, L. J., "Acoustic Impedance of Small Orifices," *Journal of the Acoustical Society of America*, Vol. 7, No. 2, 1935, pp. 94–101.
https://doi.org/10.1121/1.1915795

[3] Ingård, U., and Labate, S., "Acoustic Circulation Effects and the Nonlinear Impedance of Orifices," *Journal of the Acoustical Society of America*, Vol. 22, No. 2, 1950, pp. 211–218.
https://doi.org/10.1121/1.1906591

[4] Avallone, F., Manjunath, P., Ragni, D., and Casalino, D., "Lattice-Boltzmann Very Large Eddy Simulation of a Multi-Orifice Acoustic Liner with Turbulent Grazing Flow," AIAA Paper 2019-2542, 2019.
https://doi.org/10.2514/6.2019-2542

[5] Zhang, Q., and Bodony, D. J., "Numerical Investigation of a Honeycomb Liner Grazed by Laminar and Turbulent Boundary Layers," *Journal of Fluid Mechanics*, Vol. 792, 2016, pp. 936–980.
https://doi.org/10.1017/jfm.2016.79

[6] Scalo, C., Bodart, J., and Lele, S. K., "Compressible Turbulent Channel Flow with Impedance Boundary Conditions," *Physics of Fluids*, Vol. 27, No. 3, 2015, Paper 035107.
https://doi.org/10.1063/1.4914099

[7] Tam, C. K., Ju, H., and Walker, B. E., "Numerical Simulation of a Slit Resonator in a Grazing Flow under Acoustic Excitation," *Journal of Sound and Vibration*, Vol. 313, No. 3-5, 2008, pp. 449–471.
https://doi.org/10.1016/j.jsv.2007.12.018

[8] Shur, M., Strelets, M., Travin, A., Suzuki, T., and Spalart, P., "Unsteady Simulations of Sound Propagation in Turbulent Flow Inside a Lined Duct," *AIAA Journal*, 2021, pp. 1–17.
https://doi.org/10.2514/1.J060181

[9] Pereira, L., Bonomo, L., Quintino, N., da A. R., Silva, Cordioli, J. A., and Avallone, F., "Validation of High-Fidelity Numerical Simulations of Acoustic Liners under Grazing Flow," AIAA Paper 2023-3503, 2023.
https://doi.org/10.2514/6.2023-3503

[10] Howerton, B. M., and Jones, M. G., "Acoustic Liner Drag: A Parametric Study of Conventional Configurations," AIAA Paper 2015-2230, 2015.
https://doi.org/10.2514/6.2015-2230

[11] Howerton, B. M., and Jones, M. G., "Acoustic Liner Drag: Measurements on Novel Facesheet Perforate Geometries," AIAA Paper 2016-2979, 2016.
https://doi.org/10.2514/6.2016-2979

[12] Howerton, B. M., and Jones, M. G., "A Conventional Liner Acoustic/Drag Interaction Benchmark Database," AIAA Paper 2017-4190, 2017.
https://doi.org/10.2514/6.2017-4190

[13] Shahzad, H., Hickel, S., and Modesti, D., "Permeability and Turbulence over Perforated Plates," *Flow Turbulence and Combustion*, Vol. 109, No. 4, 2022, pp. 1241–1254.
https://doi.org/10.1007/s10494-022-00337-7

[14] Shahzad, H., Hickel, S., and Modesti, D., "Turbulence and Added Drag over Acoustic Liners," *Journal of Fluid Mechanics*, Vol. 965, 2023, Paper A10.
https://doi.org/10.1017/jfm.2023.397

[15] Shahzad, H., Hickel, S., and Modesti, D., "Physics-Informed Acoustic Liner Optimization: Balancing Drag and Noise," *AIAA Journal*, Vol. 62, No. 8, 2024, pp. 3018–3026.
https://doi.org/10.2514/1.J063677

[16] Malmary, C., Carbonne, S., Auregan, Y., and Pagneux, V., "Acoustic Impedance Measurement with Grazing Flow," AIAA Paper 2001-2193, 2001.
https://doi.org/10.2514/6.2001-2193

[17] Jing, X., Sun, X., Wu, J., and Meng, K., "Effect of Grazing Flow on the Acoustic Impedance of an Orifice," *AIAA Journal*, Vol. 39, No. 8, 2001, pp. 1478–1484.
https://doi.org/10.2514/2.1498

[18] Eldredge, J. D., and Dowling, A. P., "The Absorption of Axial Acoustic Waves by a Perforated Liner with Bias Flow," *Journal of Fluid Mechanics*, Vol. 485, 2003, pp. 307–335.
https://doi.org/10.1017/S0022112003004518

[19] Zhang, X., and Cheng, L., "Acoustic Impedance of Micro-Perforated Panels in a Grazing Flow," *Journal of the Acoustical Society of America*, Vol. 145, No. 4, 2019, pp. 2461–2469.
https://doi.org/10.1121/1.5098785

[20] Nayfeh, A., Kaiser, J., and Shaker, B., "Effect of Mean-Velocity Profile Shapes on Sound Transmission Through Two-Dimensional Ducts," *Journal of Sound and Vibration*, Vol. 34, No. 3, 1974, pp. 413–423.
https://doi.org/10.1016/S0022-460X(74)80320-2

[21] Gabard, G., "A Comparison of Impedance Boundary Conditions for Flow Acoustics," *Journal of Sound and Vibration*, Vol. 332, No. 4, 2013, pp. 714–724.
https://doi.org/10.1016/j.jsv.2012.10.014

[22] Gabard, G., "Boundary Layer Effects on Liners for Aircraft Engines," *Journal of Sound and Vibration*, Vol. 381, 2016, pp. 30–47.
https://doi.org/10.1016/j.jsv.2016.06.032

[23] Avallone, F., and Casalino, D., "Acoustic-Induced Velocity in a Multi-Orifice Acoustic Liner Grazed by a Turbulent Boundary Layer," AIAA Paper 2021-2169, 2021.
https://doi.org/10.2514/6.2021-2169

[24] Jones, M., Watson, W., and Nark, D., "Effects of Flow Profile on Educed Acoustic Liner Impedance," AIAA Paper 2010-3763, 2010.
https://doi.org/10.2514/6.2010-3763

[25] Elliott, W. P., "The Growth of the Atmospheric Internal Boundary Layer," *EOS, Transactions American Geophysical Union*, Vol. 39, No. 6, 1958, pp. 1048–1054.
https://doi.org/10.1029/TR039i006p01048

[26] Cheng, H., and Castro, I. P., "Near-Wall Flow Development After a Step Change in Surface Roughness," *Boundary-Layer Meteorology*, Vol. 105, No. 3, 2002, pp. 411–432.
https://doi.org/10.1023/A:1020355306788

[27] Rouhi, A., Chung, D., and Hutchins, N., "Direct Numerical Simulation of Open-Channel Flow over Smooth-to-Rough and Rough-to-Smooth Step Changes," *Journal of Fluid Mechanics*, Vol. 866, 2019, pp. 450–486.
https://doi.org/10.1017/jfm.2019.84

[28] Li, M., de Silva, C. M., Chung, D., Pullin, D. I., Marusic, I., and Hutchins, N., "Modelling the Downstream Development of a Turbulent Boundary Layer Following a Step Change of Roughness," *Journal of Fluid Mechanics*, Vol. 949, 2022, Paper A7.
https://doi.org/10.1017/jfm.2022.731

[29] Efros, V., and Krogstad, P.-Å., "Development of a Turbulent Boundary Layer After a Step from Smooth to Rough Surface," *Experiments in Fluids*, Vol. 51, No. 6, 2011, pp. 1563–1575.
https://doi.org/10.1007/s00348-011-1167-2

[30] Efstathiou, C., and Luhar, M., "Mean Turbulence Statistics in Boundary Layers over High-Porosity Foams," *Journal of Fluid Mechanics*, Vol. 841, 2018, pp. 351–379.
https://doi.org/10.1017/jfm.2018.57

[31] Bernardini, M., Modesti, D., Salvadore, F., Sathyanarayana, S., Della Posta, G., and Pirozzoli, S., "STREAmS-2.0: Supersonic Turbulent Accelerated Navier-Stokes Solver Version 2.0," *Computer Physics Communications*, Vol. 285, 2023, Paper 108644.
https://doi.org/10.1016/j.cpc.2022.108644

[32] Bernardini, M., Modesti, D., Salvadore, F., and Pirozzoli, S., "STREAmS: A High-Fidelity Accelerated Solver for Direct Numerical Simulation of Compressible Turbulent Flows," *Computer Physics Communications*, Vol. 263, 2021, Paper 107906.
https://doi.org/10.1016/j.cpc.2021.107906

[33] Cardillo, J., Chen, Y., Araya, G., Newman, J., Jansen, K., and Castillo, L., "DNS of a Turbulent Boundary Layer with Surface Roughness," *Journal of Fluid Mechanics*, Vol. 729, 2013, pp. 603–637.
https://doi.org/10.1017/jfm.2013.326

[34] Liu, X., Zhao, H., Luo, K., and Fan, J., "Direct Numerical Simulation of Turbulent Boundary Layer over Hemispherical Rough Walls," *International Journal of Multiphase Flow*, Vol. 83, 2016, pp. 128–141.
https://doi.org/10.1016/j.ijmultiphaseflow.2016.03.009

[35] Chung, D., Chan, L., MacDonald, M., Hutchins, N., and Ooi, A., "A Fast Direct Numerical Simulation Method for Characterising Hydraulic Roughness," *Journal of Fluid Mechanics*, Vol. 773, 2015, pp. 418–431.
https://doi.org/10.1017/jfm.2015.230

[36] MacDonald, M., Chung, D., Hutchins, N., Chan, L., Ooi, A., and García-Mayoral, R., "The Minimal-Span Channel for Rough-Wall Turbulent Flows," *Journal of Fluid Mechanics*, Vol. 816, 2017, pp. 5–42.
https://doi.org/10.1017/jfm.2017.69

[37] Di Giorgio, S., Leonardi, S., Pirozzoli, S., and Orlandi, P., "On the Relationship Between Drag and Vertical Velocity Fluctuations in Flow over Riblets and Liquid Infused Surfaces," *International Journal of Heat and Fluid Flow*, Vol. 86, 2020, Paper 108663.
https://doi.org/10.1016/j.ijheatfluidflow.2020.108663

[38] Yang, J., Stroh, A., Chung, D., and Forooghi, P., "Direct Numerical Simulation-Based Characterization of Pseudo-Random Roughness in Minimal Channels," *Journal of Fluid Mechanics*, Vol. 941, 2022, Paper A47.
https://doi.org/10.1017/jfm.2022.331

[39] Pirozzoli, S., and Colonius, T., "Generalized Characteristic Relaxation Boundary Conditions for Unsteady Compressible Flow Simulations," *Journal of Computational Physics*, Vol. 248, 2013, pp. 109–126.
https://doi.org/10.1016/j.jcp.2013.04.021

[40] Musker, A., "Explicit Expression for the Smooth Wall Velocity Distribution in a Turbulent Boundary Layer," *AIAA Journal*, Vol. 17, No. 6, 1979, pp. 655–657.
https://doi.org/10.2514/3.61193

[41] Pirozzoli, S., Bernardini, M., and Grasso, F., "Direct Numerical Simulation of Transonic Shock/Boundary Layer Interaction Under

Conditions of Incipient Separation," *Journal of Fluid Mechanics*, Vol. 657, 2010, pp. 361–393.
https://doi.org/10.1017/S0022112010001710

[42] Ceci, A., Palumbo, A., Larsson, J., and Pirozzoli, S., "Numerical Tripping of High-Speed Turbulent Boundary Layers," *Theoretical and Computational Fluid Dynamics*, Vol. 36, No. 6, 2022, pp. 865–886.
https://doi.org/10.1007/s00162-022-00623-0

[43] Vanna, F. D., Picano, F., and Benini, E., "A Sharp-Interface Immersed Boundary Method for Moving Objects in Compressible Viscous Flows," *Computers & Fluids*, Vol. 201, 2020, Paper 104415.
https://doi.org/10.1016/j.compfluid.2019.104415

[44] Vinuesa, R., Prus, C., Schlatter, P., and Nagib, H. M., "Convergence of Numerical Simulations of Turbulent Wall-Bounded Flows and Mean Cross-Flow Structure of Rectangular Ducts," *Meccanica*, Vol. 51, No. 12, 2016, pp. 3025–3042.
https://doi.org/10.1007/s11012-016-0558-0

[45] Rego, L., Avallone, F., Ragni, D., Casalino, D., and Denayer, H., "Acoustic Liners for Jet-Installation Noise Reduction," *Journal of Sound and Vibration*, Vol. 537, 2022, Paper 117189.
https://doi.org/10.1016/j.jsv.2022.117189

[46] Li, L., Liu, Y., Zhang, F., and Sun, Z., "Several Explanations on the Theoretical Formula of Helmholtz Resonator," *Advances in Engineering Software*, Vol. 114, 2017, pp. 361–371.
https://doi.org/10.1016/j.advengsoft.2017.08.004

[47] Jordi, B. E., Cotter, C. J., and Sherwin, S. J., "Encapsulated Formulation of the Selective Frequency Damping Method," *Physics of Fluids*, Vol. 26, No. 3, 2014, Paper 034101.
https://doi.org/10.1063/1.4867482

[48] Casacuberta, J., Groot, K. J., Tol, H. J., and Hickel, S., "Effectivity and Efficiency of Selective Frequency Damping for the Computation of Unstable Steady-State Solutions," *Journal of Computational Physics*, Vol. 375, 2018, pp. 481–497.
https://doi.org/10.1016/j.jcp.2018.08.056

[49] Kuwata, Y., and Suga, K., "Lattice Boltzmann Direct Numerical Simulation of Interface Turbulence over Porous and rough Walls," *International Journal of Heat and Fluid Flow*, Vol. 61, 2016, pp. 145–157.
https://doi.org/10.1016/j.ijheatfluidflow.2016.03.006

[50] Endrikat, S., Modesti, D., García-Mayoral, R., Hutchins, N., and Chung, D., "Influence of Riblet Shapes on the Occurrence of Kelvin–Helmholtz Rollers," *Journal of Fluid Mechanics*, Vol. 913, 2021, Paper A37.
https://doi.org/10.1017/jfm.2021.2

[51] Orlandi, P., and Leonardi, S., "DNS of Turbulent Channel Flows with Two- and Three-Dimensional Roughness," *Journal of Turbulence*, Vol. 7, 2006, Paper N73.
https://doi.org/10.1080/14685240600827526

[52] Wilkinson, S., "Influence of Wall Permeability on Turbulent Boundary-Layer Properties," AIAA Paper 1983-294, 1983.
https://doi.org/10.2514/6.1983-294

[53] Suga, K., Nakagawa, Y., and Kaneda, M., "Spanwise Turbulence Structure over Permeable Walls," *Journal of Fluid Mechanics*, Vol. 822, 2017, pp. 186–201.
https://doi.org/10.1017/jfm.2017.278

[54] Endrikat, S., Modesti, D., García-Mayoral, R., Hutchins, N., and Chung, D., "Influence of Riblet Shapes on the Occurrence of Kelvin-Helmholtz Rollers," *Journal of Fluid Mechanics*, Vol. 913, 2021, Paper A37.
https://doi.org/10.1017/jfm.2021.2

[55] Schlichting, H., and Gersten, K., *Boundary-Layer Theory*, 9th ed., Springer, Berlin, 1968.
https://doi.org/10.1007/978-3-662-52919-5

[56] Eitel-Amor, G., Örlü, R., and Schlatter, P., "Simulation and Validation of a Spatially Evolving Turbulent Boundary Layer up to Re_θ=8300," *International Journal of Heat and Fluid Flow*, Vol. 47, 2014, pp. 57–69.
https://doi.org/10.1016/j.ijheatfluidflow.2014.02.006

[57] Nikuradse, J., "Strömungsgesetze in Rauhen Rohren," VDI-Forschungsheft, Vol. 361, 1933.

[58] Colebrook, C. F., "Turbulent Flow in Pipes, with Particular Reference to the Transition Region Between the Smooth and Rough Pipe Laws," *Journal of the Institution of Civil Engineers*, Vol. 11, No. 4, 1939, pp. 133–156.
https://doi.org/10.1680/ijoti.1939.13150

P. Tucker
Associate Editor